Robustness of quantitative compressive sensing MRI: The effect of random undersampling patterns on derived parameters for DCE- and DSC-MRI

David. S. Smith, *Member, IEEE*, Xia Li, James V. Gambrell, Lori R. Arlinghaus, C. Chad Quarles, Thomas E. Yankeelov, and E. Brian Welch, *Member, IEEE*

Abstract—Compressive sensing (CS) in Cartesian magnetic resonance imaging (MRI) involves random partial Fourier acquisitions. The random nature of these acquisitions can lead to variance in reconstruction errors. In quantitative MRI, variance in the reconstructed images translates to an uncertainty in the derived quantitative maps. We show that for a spatially regularized $2\times$-accelerated human breast CS DCE-MRI acquisition with a 192^2 matrix size, the coefficients of variation (CoVs) in voxel-level parameters due to the random acquisition are 1.1%, 0.96%, and 1.5% for the tissue parameters K^{trans}, v_{e}, and v_{p}, with an average error in the mean of -2.5%, -2.0%, and -3.7%, respectively. Only 5% of the acquisition schemes had a systematic underestimation larger than than 4.2%, 3.7%, and 6.1%, respectively. For a $2\times$-accelerated rat brain CS DSC-MRI study with a 64^2 matrix size, the CoVs due to the random acquisition were 19%, 9.5%, and 15% for the cerebral blood flow and blood volume and mean transit time, respectively, and the average errors in the tumor mean were 9.2%, 0.49%, and -7.0%, respectively. Across 11 000 different CS reconstructions, we saw no outliers in the distribution of parameters, suggesting that, despite the random undersampling schemes, CS accelerated quantitative MRI may have a predictable level of performance.

I. INTRODUCTION

QUANTITATIVE dynamic magnetic resonance imaging (MRI) uses an injected contrast agent (CA) coupled with dynamic imaging to illuminate tissue properties. Two of the most common methods are dynamic contrast enhanced MRI (DCE-MRI) and dynamic susceptibility contrast MRI (DSC-MRI).

DCE-MRI involves the injection of a paramagnetic CA, such as Gd-DTPA (gadopentetate dimeglumine), to alter the T_1 longitudinal magnetization relaxation rate of the tissue while acquiring serial images as the contrast enters and exits the field of view. This is often used to interrogate the vascular status of tumors [5], [34], and DCE-MRI has successfully been applied to assess vascular characteristics in both preclinical and clinical settings (see, e.g., [13], [21], [24], [35]). Quantitative DCE-MRI seeks to derive, for each voxel, three pharmacokinetic parameters: K^{trans}, v_{e}, and v_{p}, which describe the contrast agent extravasation rate, the extravascular

extracellular volume fraction, and the plasma volume fraction, respectively.

DSC-MRI involves injection of a CA, such as Gd-DTPA or iron oxide nanoparticles, to dynamically alter the T_2^* transverse relaxation rate of tissues (see, e.g., [11], [27], [29], [30]). DSC-MRI is often used to assess the hemodynamic status of tissues. Quantitative DSC-MRI seeks to derive three hemodynamic parameters: the cerebral blood flow (CBF), cerebral blood volume (CBV), and mean transit time (MTT).

Quantitative dynamic MRI requires (1) *high temporal resolution* to capture the rapid contrast changes, (2) *high spatial resolution* to detect small features and accurately delineate boundaries, and (3) *high signal-to-noise ratios* to reduce uncertainties in the fits of quantitative model parameters. With such severe constraints, quantitative dynamic MRI could benefit greatly from lower data acquisition requirements. Clinically, faster sampling could allow accurate arterial input function estimation or application of tracer kinetic models that require higher temporal resolution than is currently available. Also, tumor heterogeneity analyses [17] could benefit if SNR could be increased without compromising spatial resolution.

A compressive sensing (CS) MRI [23] reconstruction is a constrained reconstruction in which the resulting image is chosen such that it has the sparsest representation possible in some basis while still being consistent with the collected Fourier data. CS can dramatically accelerate MRI data acquisitions, with, typically, an insignificant image quality loss [23]. To date, CS MRI has been tested mostly in applications relying on image morphology (e.g. [28], [31]). Quantitative CS MR is beginning to be explored (e.g. [6], [16], [32]), but no work has yet addressed the additional uncertainty in quantitative parameters due to random sampling.

Test-retest studies are one way to characterize intrapatient variance in derived quantitative maps. Such studies for DCE-MRI have found coefficients of variation (CoVs) for K^{trans} and v_{e} of 7.7% and 6.2%, respectively, in glioma [12] and 29% and 9%, respectively, in a variety of cancers [8]. A similar study for DSC-MRI [15] found a CoV of 12% in the CBV, with a correlation between scans of 0.84 ($p < 0.0001$).

Here we present a framework for exploring the variance that the random nature of the partial Fourier acquisition of CS MRI introduces into the derived parameters for quantitative DCE- and DSC-MRI.

II. Materials and Methods

A. Human DCE-MRI

1) Data: Ten patients with locally advanced breast cancer were enrolled in an ongoing clinical trial. The patients provided informed consent, and the study was approved by the ethics committee of our Institute. DCE-MRI data were acquired using a Philips 3T Achieva MR scanner[1] using a four-channel receive bilateral breast coil.[2] For each patient, two data sets were sequentially acquired: one for constructing a T_1 map and one for the DCE-MRI analysis.

Data for constructing a T_1 map were acquired using a 3D gradient echo multiple flip angle approach with $T_R = 7.9$ ms, $T_E = 1.3$ ms, and flip angles of 2 to 20 degrees in two degree increments. Uniform flip angle spacing was used instead of an optimized set [33] because of the broad range of tissue T_1 values found in typical tumor tissue. The acquisition matrix was $192 \times 192 \times 20$ (full-breast) over a sagittally oriented field of view of 22 cm $\times$ 22 cm $\times$ 10 cm. Scan time was just under three minutes.

The dynamic sequences used identical parameters but with a single flip angle of 20 deg. Each 20-slice set was collected in 16.5 seconds at 25 time points for approximately seven minutes of scanning. A catheter placed within an antecubital vein delivered 0.1 mmol/kg of the contrast agent Magnevist[3] at 2 mL/s (followed by a saline flush) via a power injector[4] after the acquisition of three baseline dynamic scans for the DCE study. An individual AIF was obtained from the axillary artery of each patient as previously reported [19].

2) Analysis: Data collected at multiple flip angles for the T_1 map were fit using a trust-region-reflective, nonlinear least squares algorithm (Matlab's lsqcurvefit) to the gradient echo signal intensity equation

$$S(t) = S_0 \sin \alpha \frac{1 - \exp\left[-T_R/T_1(t)\right]}{1 - \cos \alpha \exp\left[-T_R/T_1(t)\right]}, \quad (1)$$

where α is the flip angle, S_0 is a constant describing the scanner gain and proton density, and we have assumed that $T_E \ll T_2^*$, where T_E is the echo time.

To derive pharmacokinetic parameters, T_1 can be related linearly to the concentration of CA in the tissue, $C_t(t)$, by

$$1/T_1(t) = r_1 C_t(t) + 1/T_1(0), \quad (2)$$

where $T_1(0)$ is the T_1 of the tissue before CA administration (obtained from the T_1 mapping sequence), $T_1(t)$ is the T_1 relaxation during the dynamic sequence, and r_1 is the CA relaxivity. The extended Kety relationship [18] is then used to derive tissue parameters:

$$C_t(t) = v_p C_p(t) + K^{\text{trans}} \times \int_0^t C_p(t') \exp\left[-K^{\text{trans}}(t - t')/v_e\right] dt', \quad (3)$$

where K^{trans} is the CA extravasation rate constant, v_e is the extravascular extracellular volume fraction, v_p is the plasma
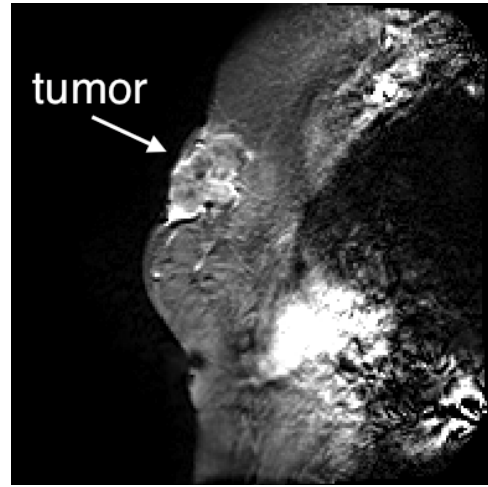

Fig. 1. Sagittal slice from the full breast DCE data set (anterior-posterior direction is left-right, superior-inferior is up-down). The tumor is indicated by the arrow and is brighter than the surrounding tissue after having been perfused with blood containing the Gd contrast agent. The bright region at the lower right is an artifact due to the heart.

fraction, and $C_p(t)$ is the concentration of CA in blood plasma. $C_p(t)$ is known as the arterial input function (AIF).

For each of the ten patients, three DCE parameters were derived for each voxel in the tumor using both the full data set and a $2\times$-accelerated CS data set. The $2\times$ CS data set was generated by randomly selecting phase encodes according to the prescription below in §II-C. The tumor-wide means and voxel-level correlation of the derived parameters from the full and CS data were examined, and the median data was selected for further study. Figure 1 shows an example slice from the full data set of the selected patient.

The second phase of the study involved performing retrospective CS acquisitions on the selected "typical" data set. Only $2\times$ CS acceleration was considered. The fully sampled Fourier data was generated from reconstructed magnitude images. The protocol used for this study captured only a partial echo, so the full complex reconstructed images were not available. One thousand realizations of a $2\times$ phase encode scheme for the image resolution (192^2) were generated. This subsampling scheme was then applied to the full data set, and the resulting partial data set was reconstructed with a 2-D Cartesian CS MRI reconstruction scheme. This scheme is explained in detail in §II-C. DCE parameter triplets were then derived for each voxel for each of these 1000 CS reconstructions, and the resulting values compared to the parameters derived from the full data set.

B. Rat DSC-MRI

1) Data: DSC-MRI data was acquired using a Varian 4.7 T small animal MR scanner[5] equipped with a 63 mm quadrature birdcage coil. During the experiment, a warm flow of air over the animal maintained the body temperature at 37° C. The respiratory rate was monitored throughout the experiment and maintained at 40–60 breaths per minute. After tumor

---

[1]Philips Healthcare, Best, The Netherlands
[2]Invivo, Inc., Gainesville, FL
[3]Bayer, Wayne, NJ
[4]MEDRAD, Warrendale, PA

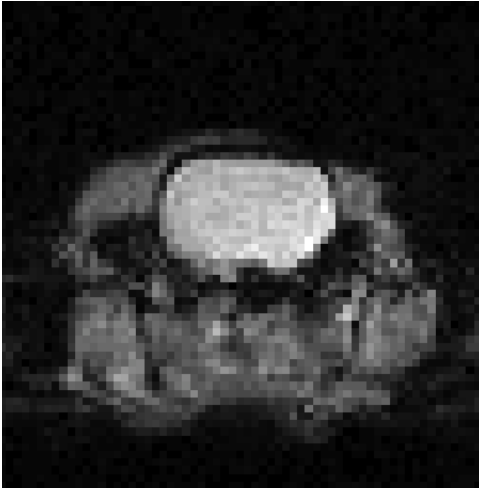[5]Varian Medical Systems, Palo Alto, CA

Fig. 2.   Example image from the full DSC data set. The brain is the bright central object. A slice through the middle of the brain was used, and the entire brain was used for ROI analysis.

localization, a gradient echo planar (EPI) pulse sequence was used to acquire DSC-MRI data with the following parameters: $T_R = 0.5$ sec, $T_E = 16.1$ ms, FOV = $(40$ mm$)^2$, slice thickness = 1.5 mm, matrix = 64^2, and a flip angle = $65°$. At 60 seconds into the image acquisition a 2.5-mg/kg bolus of iron oxide CA, Molday ION,[6] was administered intravenously via a jugular catheter. All studies adhered to our institution's animal care and use committee. Figure 2 shows an example axial slice through the brain from the full DSC data set.

2) Analysis: The CA concentration time curves for each voxel were quantified with the assumption of a linear relationship between CA concentration and the change in the gradient echo transverse relaxation rate, ΔR_2^*. The ΔR_2^* times were computed as the logarithm of the MRI signal intensities:

$$\Delta R_2^* = (-1/T_E) \log[S(t)/S_0], \qquad (4)$$

where $S(t)$ is the post-contrast injection signal intensity and S_0 is the pre-contrast signal. A tracer kinetic analysis of the concentration time curves was used to compute the hemodynamic parameters as previously described [26]. The arterial input function was computed as the average transverse relaxation rate time curves over three voxels located near branches of the middle cerebral artery. Tissue residue functions were derived by deconvolving the tissue concentration time curves with the AIF using singular value decomposition [26]. The CBF was computed as the peak of the residue function, the CBV was determined as the area under the concentration time curves and the MTT was taken as the ratio of the CBV to CBF according to the central volume theorem [26].

Instead of 1000 CS acquisitions, as in the DCE-MRI study, we generated 10 000 different random CS DSC-MRI acquisitions and applied them retrospectively to the full 64^2 data set. The reasons for this will be explained in §III. Each of the 10 000 partial data sets was reconstructed with the CS MRI reconstruction scheme described in §II-C. DSC parameter triplets were then derived on one slice for each voxel

[6]BioPAL, Worcester, MA

containing healthy brain tissue for each CS reconstruction, and the resulting values were compared to the parameters derived from the full data set.

C. Compressive Sensing Reconstruction

Compressive sensing [1], [7] can accelerate MRI data acquisitions by sampling fewer spatial frequencies than required to satisfy the Nyquist-Shannon theorem. The missing data are iteratively reconstructed with a regularized least squares algorithm in which, typically, the gradient of the reconstructed image serves as a regularizer. Specifically, the reconstructed image u in compressed sensing MRI is usually a solution to the unconstrained minimization problem

$$\arg \min_u \ \|Su\|_1 + \frac{\lambda}{2}\|Fu - d\|_2^2, \qquad (5)$$

where S is a sparsity transform, such as a wavelet decomposition or the image gradient, F is the partial Fourier measurement operator, d are the scanner-collected Fourier coefficient data, and λ controls the relative weighting of the two norm terms, defined as $\|x\|_1 \equiv \sum_i |x_i|$ and $\|x\|_2^2 \equiv \sum_i x_i^2$. Note that the CS reconstruction problem, as opposed to traditional least squares problems with linear regularizers, is non-linear and has no closed-form solution.

In a Cartesian CS MRI acquisition scheme, the ability to undersample the Fourier domain is restricted to randomly omitting 1-D phase encodes, corresponding to entire rows from the Fourier matrix in 2-D or 3-D acquisitions. In the reconstructions presented here, the lowest spatial frequencies are fully sampled, while at higher frequencies the sampling density of phase encodes follows $|k|^{-0.5}$, where k is spatial frequency. The cutoff between uniform sampling and random sampling is chosen such that the total number of phase encodes in the scheme is the number determined by the acceleration. The $|k|^{-0.5}$ distribution of spatial frequency samples was empirically chosen to improve image contrast while not sacrificing too much spatial detail. A centrally biased sampling pattern improves contrast by including more of the low spatial frequencies that contain most of the image power (see, e.g., Fig. 8 of [23]). During the reconstruction, an image consistent with the measured Fourier data is sought that sparsifies its isotropic gradient, defined as

$$\nabla u = \sqrt{(u_{i,j} - u_{i,j-1})^2 + (u_{i,j} - u_{i-1,j})^2}, \qquad (6)$$

with boundaries treated periodically and each slice treated independently. It is important to note that this transform does not have a simple relationship to the desired pharmacokinetic parameters, so it is not clear that a time independent CS MRI reconstruction will retain the necessary dynamic information to retrieve accurate DCE parameters. Additionally, our data sets are relatively low resolution (192^2 and 64^2 matrix sizes), so the images are consequently less compressible under a gradient transformation. This means total variation normalized by the number of voxels will be larger, and, since the reconstruction problem is being posed as an unconstrained minimization problem, the data fidelity will be compromised more in order to produce a given level of decrease in the TV.

This article has been accepted for publication in a future issue of this journal, but has not been fully edited. Content may change prior to final publication.

IEEE TRANS. MED. IMAG., VOL. 0, NO. 0, MONTH YEAR
4

The CS reconstruction here was performed using a non-convex, total variation (TV) regularized Cartesian split Bregman algorithm [10] modified to run on a GPU workstation using Jacket 1.6.0[7] and Matlab R2010b[8]. The non-convexity comes from the use of the $\ell_{1/2}$ quasi-norm instead of the typical ℓ_1 norm of the gradient according to the prescription of [3]. Thus the optimization problem as implemented here becomes

$$\arg \min_{u} \ \|Su\|_{1/2}^{1/2} + \frac{\lambda}{2}\|Fu - d\|_2^2, \qquad (7)$$

where $\|x\|_{1/2}^{1/2} \equiv \sum_i \sqrt{|x_i|}$.

As shown in [3], this modification to the basic CS MRI reconstruction algorithm improves image quality and reduces artifacts. With a non-convex optimization problem, however, the reconstructed image is no longer assured to be a global optimum, but for quantitative MRI a solution that maintains sufficient fidelity of the model parameters is all that is required. In fact, this paper is an effort to explore under what circumstances this criterion is being met. We chose $\lambda = 20$ empirically in order to reduce the spatial smoothing and stair stepping that can occur with TV minimization.

D. Statistical Analysis

Concordance correlation coefficients (CCCs; [20]), region-of-interest (ROI) means, and coefficients of variation (CoVs) were used as the measures of agreement between sets of quantitative parameters derived from the fully sampled and undersampled data. CCCs measure the extent to which the three parameters for a given voxel in the CS reconstruction are equal to of those in the fully sampled data set. CoVs were defined as the ratio of the standard deviation of the CS parameter sets to their means and given in percent.

III. RESULTS

A. Human Quantitative DCE-MRI

In CS MRI, a compromise is struck between fidelity to the acquired Fourier data and the sparsity of the reconstructed image in some chosen transform domain. This leads to an additional source of uncertainty in the reconstruction problem. One definition of "well behaved" CS subsampling could be that this additional level of uncertainty is independent of the particular random Fourier sampling scheme chosen.

Figure 3 shows histograms of CCCs and tumor means for K^{trans}, v_{e}, and v_{p} from the 1000 CS DCE-MRI data sets. All three parameters have similar CCCs and tumor means across all 1000 acquisition schemes, suggesting that despite the random nature of the phase encode scheme the end results—the quantitative parameters—are consistent.

As is to be expected when decimating magnitude images, the low acceleration factor, 2×, used here produces excellent agreement with the full data set for almost all reconstructions. The significant new feature of these results is the variance in agreement across the range of random undersampling patterns. The horizontal lines above the histograms show the 5-95%

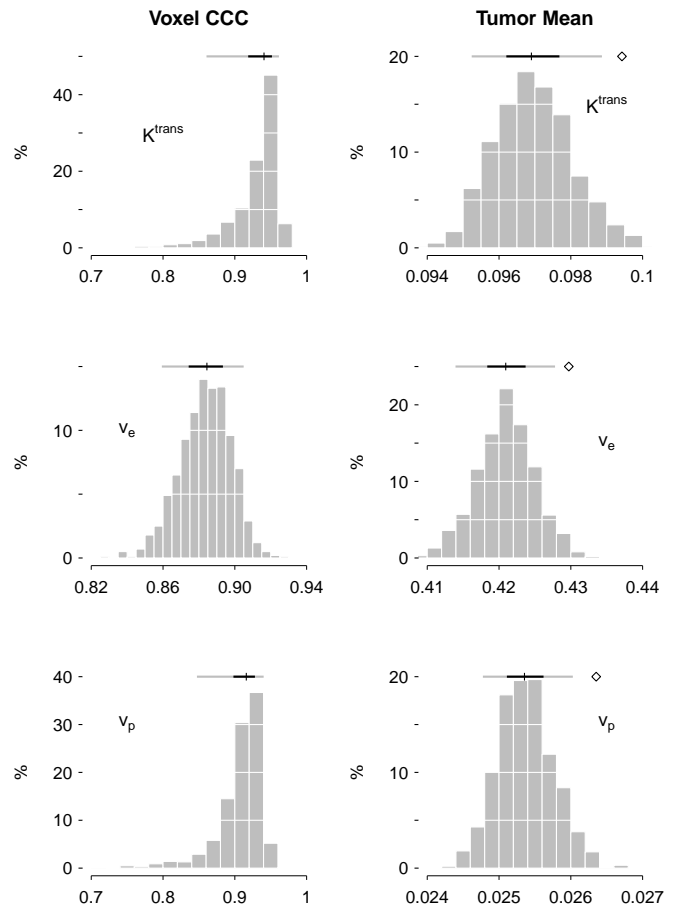[7]AccelerEyes, Atlanta, GA
[8]Mathworks, Natick, MA

Fig. 3. Results of 1000 different simulated CS DCE-MRI acquisitions. Above each histogram, the horizontal line shows the 5–95% quantile in gray, the 25–75% in black and the mean by the vertical tick. For tumor mean parameters, the open diamond above the histograms shows the mean parameter value for the model that used the full data set. All three parameters are systematically underestimated by a few percent on average. The variance is small and the distributions of results have a normal character, which means that CS undersampling has a relatively predictable outcome for this experiment.

range in gray, the 25-75% range in black, and the mean by the vertical tick. For tumor means, the mean derived from the full data set is indicated by the open diamonds. For 95% of the acquisition schemes, the CCCs for K^{trans}, v_{e}, and v_{p} were greater than 0.86, 0.86, and 0.85, respectively, and the tumor means of K^{trans}, v_{e}, and v_{p} were underestimated by less than 4.2%, 3.7%, and 6.1%, respectively. The CoVs were 1.1%, 0.96%, and 1.5%, respectively.

For this 192^2 data set, we used a 2× undersampling and a $|k|^{-0.5}$ probability distribution to choose the random phase encode subsets. A fully sampled center window of width 16 was always chosen to ensure that the lowest frequencies were always acquired, which increases total signal. This left 80 phase encode lines left to be chosen and 176 unused frequencies from which to take them. Thus there are theoretically $\binom{192-16}{96-16} = 2.8 \times 10^{51}$ unique random phase encode schemes possible. The nearly normal character of the distributions after just 1000 trials, however, suggests that the results here are representative of the full gamut of acquisitions.

It is evident that despite the small variance in tumor means
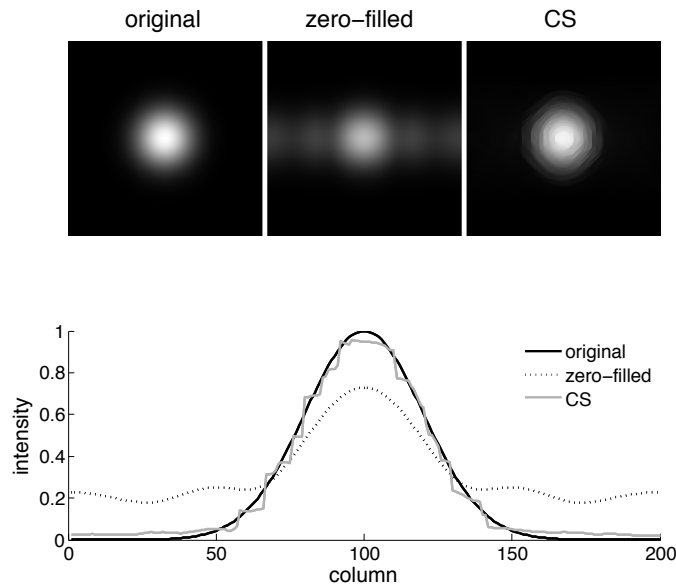
original   zero−filled   CS

Fig. 4. Example of intensity loss in a bright object on a dark background. The test images are shown above a horizontal cut through the center of the images. The CS reconstruction retrieves most of the intensity, but some underestimation of the central peak and overestimation of the periphery remains.

there is a systematic underestimation. In fact, almost every CS reconstruction underestimates all three parameters. This is likely due to a slight loss of contrast in the tumor, perhaps due to the gradient shrinkage used in the CS reconstruction.

Figure 4 demonstrates the nature of the contrast loss inherent in a CS reconstruction. The original 200^2 image consists of circular object with a Gaussian intensity profile. Undersampling by a factor of six according to the same $|k|^{-0.5}$ sampling density and then filling the missing data with zeros produces periodic errors in the phase encode direction and a significant loss of contrast in the central region. In addition to the local intensity loss, the total image intensity must be less than before because power was lost in the Fourier domain and power is conserved by a Fourier transform according to Parseval's theorem. The nonconvex CS reconstruction retrieves most of the power in the object, but there is still a small underestimation of the peak and some stair stepping on the edges due to the gradient minimization. The leakage of intensity away from the central, bright object is also evident by the brighter tails of the horizontal cuts in the CS and zero-filled cases.

If the inverse image were used in the experiment in Fig. 4, one can easily demonstrate that the optimization problem would produce an overestimation of the intensity in a small dark region. Any quantitative CS MRI that measures properties of regions that are either much brighter or much darker than the surrounding image could be affected by such intensity under- and over-estimations, respectively. In particular, an enhancing DCE-MRI voxel-intensity time course should be flattened relative to that of a neighboring unenhanced voxel.

To see what effect the systematic parameter underestimation of the CS reconstructions would have on the voxel-intensity time courses, we modeled two time courses: one using the

DCE parameters from the full data set and one with all parameters decreased by 3%, which is representative of a typical CS data set from Fig. 3. Figure 5 shows the results of this model. The upper panel of Fig. 5 shows the two time courses overlain. The small underestimate of the model parameters corresponds into a similar error in the intensity time course.

To attempt to elucidate this behavior, we present in the lower panel of Fig. 5 a simple linear model for the difference between the CS and full time course along with the actual difference. The linear model assumes that, at the first time point, there is no difference between the tumor and the background, while at the peak of the time course the intensity is maximally underestimated, with a linear change in underestimation in between. The agreement between the curves is not perfect, but the general character is the same. This suggests that the intensity underestimation of a bright ROI by the CS reconstruction is in fact dependent on the relative contrast of the ROI. Also, the magnitude of underestimation of the peak intensity of the time course is 1.5%, which is of the same order as the underestimation of the derived DCE parameters (3%).

B. Rat Quantitative DSC-MRI

Figure 6 shows histograms of 10 000 different simulated CS DSC-MRI parameters sets. The horizontal lines above the histograms show the 5-95% range in gray, the 25-75% range in black, and the mean by the vertical tick. For tumor means, the mean derived from the full data set is indicated by the open diamonds. For 95% of the acquisition schemes, the CCCs for CBF, CBV, and MTT were greater than 0.78, 0.85, and 0.21, respectively, and the means of the tumor means for were within 9.2%, 0.49%, and -7.0%, respectively, of those for the full data set. The CoVs were 19%, 9.5%, and 15%, respectively. The CBV seems to be the least affected by CS acceleration.

We believe the agreement on the DSC-MRI data is worse than for DCE-MRI because the image resolution is lower by a factor of three in each direction. A lower-resolution anatomical image is less compressible under a gradient transformation, so the CS reconstruction is less able to constrain missing data. This is related to the so-called "blessing of high-dimensionality" (see, e.g., [1]).

For this 64^2 data set, we used a $2\times$ undersampling, probability distribution of $|k|^{-0.5}$, and center window width of 6, so there are theoretically $\binom{64-6}{32-6} = 2.2 \times 10^{16}$ different phase encode schemes possible. With 10 000 realizations of the random phase encode schemes, the concern again is whether this is a representative sample of the parameter space. Figure 7 shows the histograms of parameters from the first 1000 acquisition schemes from the full set of 10 000 shown in Fig. 6. This was actually our initial experiment, but the bimodal character of the histograms suggested that a larger sample was needed. It is clear, however, by the similarity of Figs. 6 and 7 that the sample statistics are representative even with just 1000 data sets because the histograms are nearly identical for all three parameters.
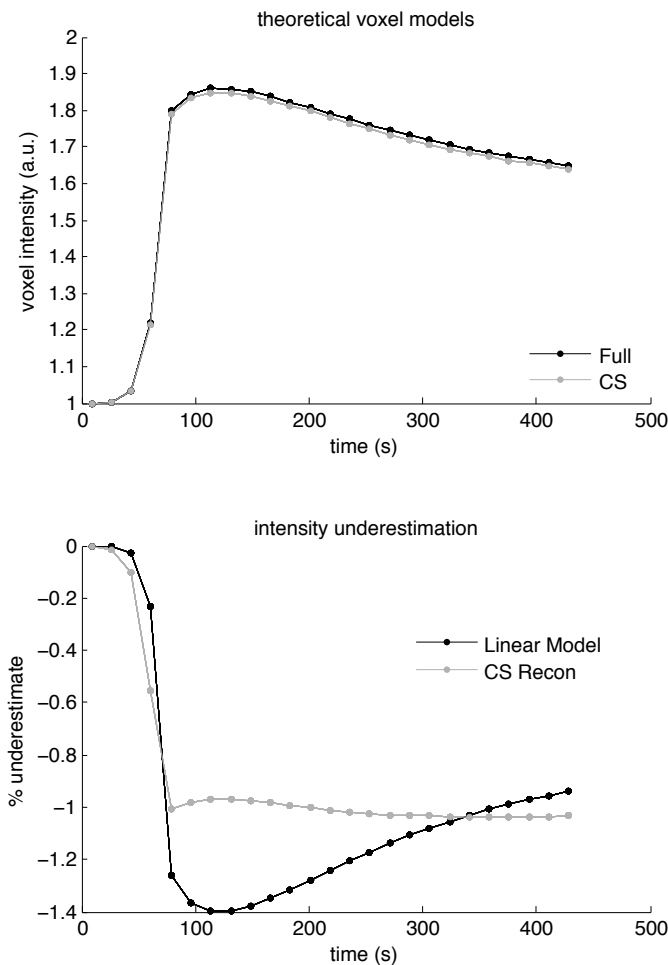
Fig. 5. Model for CS systematic underestimation of DCE parameters. The upper graph shows two theoretical DCE voxel time courses: one with K^{trans}, v_{p}, and v_{e} set to the mean from the full breast data set (labeled "Full") and one with those same parameters all decreased by 3% (labeled "CS"). The effect on the voxel-intensity time course is slight. The lower graph compares the relative intensity loss at each time point between the full and CS curves in the top graph (labeled "CS Recon") and the intensity loss if the voxel intensity were underestimated linearly by the CS reconstruction (labeled "Linear Model"). This linear intensity underestimation in the model assumes no intensity loss pre-contrast and a linear increase in intensity loss that is a maximum at time of peak contrast. The trend is similar to the intensity loss seen in the real CS reconstruction, which is consistent with a contrast-dependent intensity loss, but perhaps a nonlinear functional dependency.

Fig. 6. Result of 10 000 different random simulated CS DSC-MRI acquisitions. The 5–95% quantile in shown in gray, 25–75% in black, and the mean by a vertical tick. The open diamonds on the tumor mean histograms show the mean of the maps derived from the full data set.

IV. CONCLUSION

We have shown, for a large sample of different random CS MRI acquisition schemes, the variance in derived quantitative DCE- and DSC-MRI parameters. For DCE-MRI, with a bright tumor on a dark background and a higher resolution (192^2), the variance in parameters derived from CS acquisitions was small, but there was a systematic underestimation of 2.5%, 2.0%, and 3.7% on average for K^{trans}, v_{e}, and v_{p}, respectively. Compared to intra-patient test-retest variability [8], [12], the variation due to random CS undersampling as measured by CoVs was much smaller.

For the DSC-MRI data, with its $3\times$ lower resolution (64^2) and low contrast ROI, the parameter sets derived from the CS acquisition are characterized by a high variance but smaller error in tumo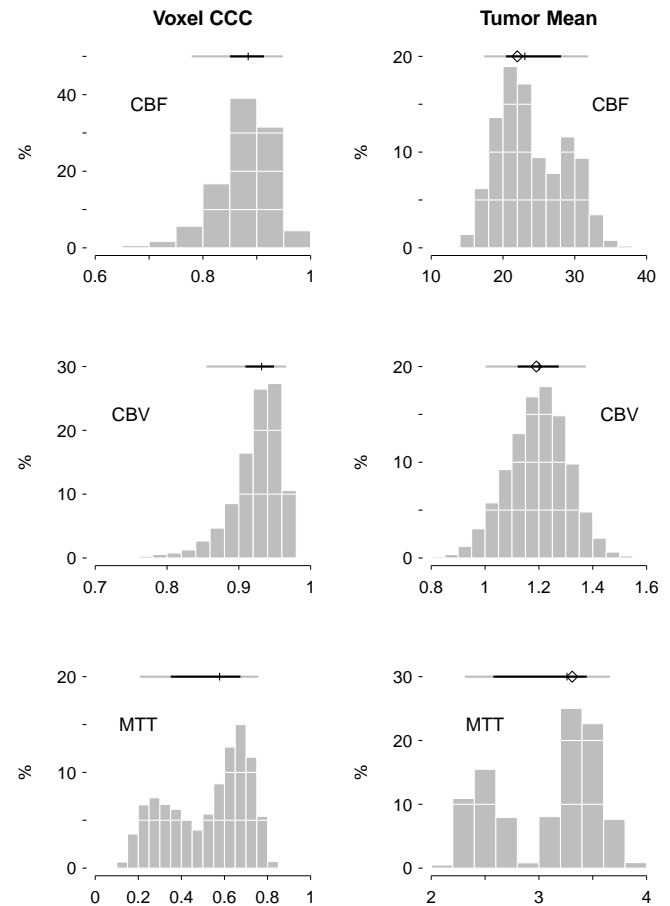r means of CBV, CBF, or MTT. The CBV was the most robust to CS acceleration and had a CoV smaller than that measured for intra-patient variability by the one test-retest study we found [15].

It is encouraging that across the 11 000 different random acquisition schemes examined here, there were no outliers in the CCCs or means. This suggests that it could be shown that, despite the random nature of CS measurements, the reconstructed data sets will have a predictable level of uncertainty. Since we are presenting here a simplified CS reconstruction scheme, we cannot predict the quantitative uncertainty level for a particular CS-accelerated DCE-MRI protocol, but we believe that the qualitative features of our approach are generic. Here we wish only to introduce a validation procedure for CS-accelerated quantitative MRI methods.

Several factors will influence the exact results from clinically practical, prospectively acquired CS-accelerated sequences. First, temporal regularization (e.g. [4], [9], [14], [22]) coupled with a time-varying undersampling pattern will likely be used. Temporal constraints, such as a temporal gradient or temporal Fourier transform serve to increase the sparsity of the reconstructed images, and the probability of recovering the correct sparse signal has been proven [2] to depend on the signal sparsity and number of measurements. A similar
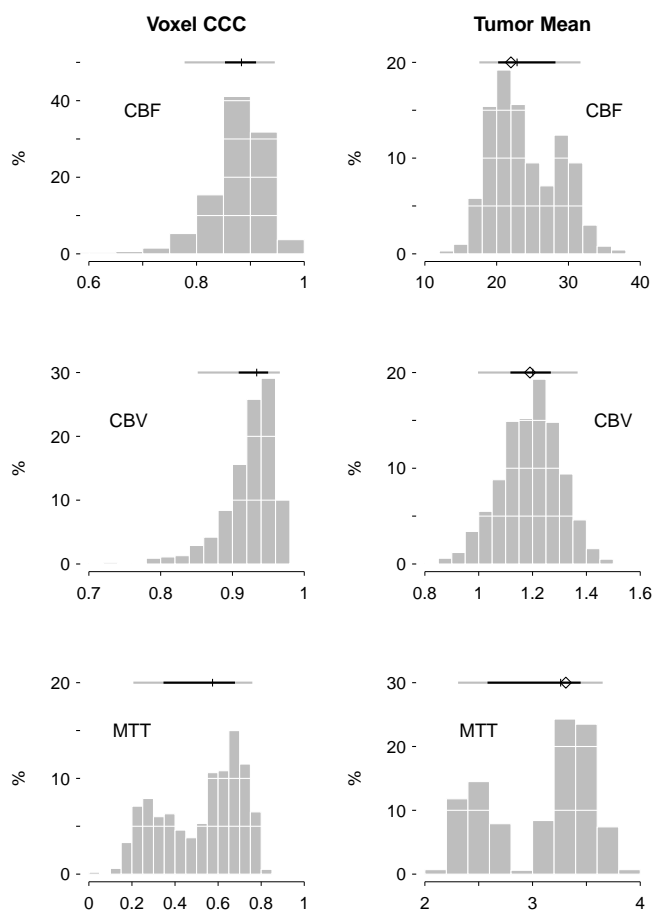
This article has been accepted for publication in a future issue of this journal, but has not been fully edited. Content may change prior to final publication.

IEEE TRANS. MED. IMAG., VOL. 0, NO. 0, MONTH YEAR 7

Fig. 7. Result of the first 1000 simulated CS DSC-MRI acquisitions from Fig. 6. The 5–95% quantile in shown in gray, 25–75% in black, and the mean by a vertical tick. The open diamonds on the tumor mean histograms show the mean of the maps derived from the full data set. The distributions are almost identical to those in Fig. 7, suggesting that the sample size is large enough that the moments of the distributions have converged.

idea may hold for compressible signals as studied here, except that rather than the probability of recovery depending on the sparsity, the recovery error would depend on the compression ratio. As an aside, the freedom to vary the undersampling pattern in time increases the size of the search space, possibly requiring more test reconstructions to explore the statistical behavior of the random undersampling.

The second major change in going to a prospective CS-accelerated acquisition is that the undersampled complex, multi-coil data set will need to be reconstructed. Signal inhomogeneities from individual coils reduce the sparsity of the coil images under a gradient or wavelet transform, possibly increasing reconstruction error, and the computational demand of the reconstruction increases linearly with the number of receive channels. Here we used reconstructed magnitude images because the scanner produced these without the need for us implementing a compute-intensive multi-channel recon. Only magnitude images were available from the MR scanner's reconstructor because the research DCE-MRI sequence acquired a partial echo during readout to reduce scan time. This is a common acceleration method that uses homodyne detection

[25] to complete k-space. Unfortunately, this method cannot produce complex images, since the phase of the Fourier data is accurately known for the lowest spatial frequencies only.

For this initial work, we chose to forgo temporal constraints and a full parallel imaging reconstruction to make this primarily exploratory work less computationally demanding. Taking just a single slice of the imaging volume, as we've done here for both datasets, we have 25 000 2-D images to reconstruct for the DCE example and 1.2 million 2-D images for the DSC example. Additionally, temporal regularizers would affect the shape of the voxel time courses and introduce a confounding factor into the variance into the derived quantitative parameters. For this initial effort, we chose a limited reconstruction problem that should capture the essential features of the issue and allow a representative sampling of the search space. We also kept the phase encode scheme constant in time because we used purely spatial regularization; temporally varying the undersampling scheme without temporal constraints would add unnecessary variance.

We would like to remark here that understanding contrast loss in CS reconstructed images will improve the prediction of the error in derived quantitative parameters. If the effect of Fourier undersampling coupled with a CS reconstruction could be known completely in image space, the predicted errors in derived quantitative maps will be straightforward to compute.

Finally, future studies should address whether CS changes the number of enhancing voxels in DCE-MRI studies. This measure can be used as a tumor size measurement, and, depending on the optimization constraints used, the spatial gradient shrinkage performed in CS MRI reconstructions can threshold small gradients to zero, effectively squashing small enhancements. This would decrease the number of enhancing voxels and hence the apparent tumor size.

REFERENCES

[1] E. J. Candès, "Compressive sampling," in *Proc. Intl. Congress Mathematicians*, Madrid, Spain, 2006, pp. 1–20.
[2] E. J. Candès, J. Romberg, T. Tao, "Robust uncertainty principles: exact signal reconstruction from highly incomplete frequency information," *IEEE Trans. Inform. Theory*, vol. 52, pp. 489–509, 2006.
[3] R. Chartrand, "Exact reconstruction of sparse signals via nonconvex minimization," *IEEE Sig. Proc. Lett.*, vol. 14, pp. 707-10, 2007.
[4] L. Chen, M. C. Schabel, E. V. R. DiBella, "Reconstruction of dynamic contrast enhanced magnetic resonance imaging of the breast with temporal constraints," *Magn. Reson. Imag.*, vol. 28, pp. 637–645, 2010.
[5] P. L. Choyke, A. J. Dwyer, and M. V. Knopp, "Functional tumor imaging with dynamic contrast-enhanced magnetic resonance imaging," *J. Magn. Reson. Imag.*, vol. 17, pp. 509-20, 2003.
[6] M. Doneva, P. Börnert, H. Eggers, C. Stehning, J. Sénégas and A. Mertins, "Compressed sensing reconstruction for magnetic resonance parameter mapping," *Magn. Reson. Med.*, vol. 64, pp. 1114–1120, 2010.
[7] D. L. Donoho, "Compressed sensing," *IEEE Trans. Inf. Theory*, vol. 52, pp. 1289-1306, 2006.
[8] S. M. Galbraith, M. A. Lodge, N. J. Taylor, G. J. S. Rustin, S. Bentzen, J. J. Stirling and A. R. Padhani, "Reproducibility of dynamic contrast-enhanced MRI in human muscle and tumours: comparison of quantitative and semi-quantitative analysis," *NMR Biomed.*, vol. 15, pp. 132–42, 2002.

[9] U. Gamper, P. Boesiger and S. Kozerke, "Compressed sensing in dynamic MRI," *Magn. Reson. Med.*, vol. 59, pp. 365–373, 2008.

[10] T. Goldstein and S. Osher, "The split Bregman method for L1 regularized problems," *SIAM J. Imag. Sci.*, vol. 2, pp. 323–43, 2009.

[11] F. Guckel, G. Brix, K. Rempp, M. Deimling, J. Rother and M. Georgi, "Assessment of cerebral blood volume with dynamic susceptibility contrast enhanced gradient-echo imaging," *J. Comput. Assist. Tomogr.*, vol. 18, pp. 344–51, 1994.

[12] A. Jackson, G. C. Jayson, K. L. Li, X. P. Zhu, D. R. Checkley, J. J. L. Tessier and J. C. Waterton, "Reproducibility of quantitative dynamic contrast-enhanced MRI in newly presenting glioma," *Brit. J. Radiology*, vol. 76, pp. 153–62, 2003.

[13] L. R. Jensen, E. M. Huuse, T. F. Bathen, P. E. Goa, A. M. Bofin, T. B. Pedersen, S. Lundgren and I. S. Gribbestad, "Assessment of early docetaxel response in an experimental model of human breast cancer using DCE-MRI, ex vivo HR MAS, and in vivo ^{1}H MRS," *NMR Biomed.*, vol. 23, pp. 56–65, 2010.

[14] H. Jung, K. Sung, K. S. Nayak, E. Y. Kim and J. C. Ye, "k-t FOCUSS: A general compressed sensing framework for high resolution dynamic MRI," *Magn. Reson. Med.*, vol. 61, pp. 103–116, 2009.

[15] M. E. Henry, M. J. Kaufman, N. Lange, M. E. Schmidt, S. Purcell, J. Cote, D. M. Perron-Henry, E. Stoddard, B. M. Cohen and P. F. Renshaw, "Test-retest reliability of DSC MRI CBV mapping in healthy volunteers," *Neuroreport*, vol. 12, pp. 1567–9, 2001.

[16] S. Hu, M. Lustig, A. Balakrishnan, P. E. Larson, R. Bok, J. Kurhanewicz, S. J. Nelson, A. Goga, J. M. Pauly and D. B. Vigneron, "3D compressed sensing for highly accelerated hyperpolarized 13C MRSI with in vivo applications to transgenic mouse models of cancer," *Magn. Reson. Med.*, vol. 63, pp. 312–312, 2010.

[17] A. Jackson, J. P. O'Connor, G. J. Parker and G. C. Jayson, "Imaging tumor vascular heterogeneity and angiogenesis using dynamic contrast-enhanced magnetic resonance imaging," *Clin. Cancer Res.*, vol. 13, pp. 3449–3459, 2007.

[18] S. S. Kety, "Peripheral blood flow measurement," *Pharmacol. Rev.*, vol. 3, pp. 1–41, 1951.

[19] X. Li, E. B. Welch, A. B. Chakravarthy, I. Mayer, M. Kelley, I. Meszoely, J. Means-Powell, J. C. Gore and T. E. Yankeelov, "A semi-automated method for obtaining the arterial input function in dynamic breast data," *Proc. Intl. Soc. Mag. Reson. Med. (ISMRM)*, p. 2729, 2010.

[20] L. I.-K. Lin, "A concordance correlation coefficient to evaluate reproducibility," *Biometrics*, vol. 45, pp. 255–68, 1989.

[21] A. C. Lockhart et al., "Phase I study of intravenous vascular endothelial growth factor trap, aflibercept, in patients with advanced solid tumors," *J. Clin. Oncol.*, vol. 28, pp. 207–14, 2010.

[22] M. Lustig, J. M. Santos, D. L. Donoho and J. M. Pauly, "k-t SPARSE: high frame rate dynamic MRI exploiting spatio-temporal sparsity," *Proc. Intl. Soc. Magn. Reson. Med.*, Seattle, WA, 2006.

[23] M. Lustig, D. Donoho and J. M. Pauly, "Sparse MRI: The application of compressed sensing for rapid MR imaging," *Mag. Reson. Med.*, vol. 58, pp. 1182–95, 2007.

[24] L. Mannelli et al., "Evaluation of nonenhancing tumor fraction assessed by dynamic contrast-enhanced MRI subtraction as a predictor of decrease in tumor volume in response to chemoradiotherapy in advanced cervical cancer," *AJR Am. J. Roentgenol.*, vol. 195, pp. 524–47, 2010.

[25] D. C. Noll, D. G. Nishimura, A. Macovski, "Homodyne detection in magnetic resonance imaging," *IEEE Trans. Med. Imag.*, vol. 10, pp. 154–63, 1991.

[26] L. Ostergaard, R. M. Weisskoff, D. A. Chesler, C. Gyldensted, B. R. Rosen, "High resolution measurement of cerebral blood flow using intravascular tracer bolus passages. Part I: Mathematical approach and statistical analysis," *Mag. Reson. Med.*, vol. 36, pp. 715–25, 1996.

[27] L. Ostergaard, "Principles of cerebral perfusion imaging by bolus tracking," *Mag. Res. Imag.*, vol. 22, pp. 710–17, 2005.

[28] R. Otazo, D. Kim, L. Axel and D. Sodickson, "Combination of compressed sensing and parallel imaging for highly accelerated first-pass cardiac perfusion MRI," *Magn. Reson. Med.*, vol. 64 pp. 767–76, 2010.

[29] K. A. Rempp, G. Brix, F. Wenz, C. R. Becker, F. Guckel and W. J. Lorenz, "Quantification of regional cerebral blood flow and volume with dynamic susceptibility contrast-enhanced MR imaging," *Radiology*, vol. 93, pp. 637–41, 1994.

[30] B. R. Rosen et al., "Contrast agents and cerebral hemodynamics," *Magn. Reson. Med.*, vol. 19, pp. 285–92, 1991.

[31] J. Trzasko, C. Haider and A. Manduca, "Practical nonconvex compressive sensing reconstruction of highly-accelerated 3D paralllel MR angiograms," *Proc. IEEE Int. Symp. Biomed. Imag.*, p. 1349, 2009.

[32] J. Velikina, A. L. Alexander and A. A. Samsonov, "A novel approach for T1 relaxometry using constrained reconstruction in parametric dimension," *Proc. ISMRM*, p. 350, 2010;

[33] H. Z. Wang, S. J. Riederer and J. N. Lee, "Optimizing the precision in T1 relaxation estimation using limited flip angles," *Magn. Reson. Med.*, vol. 5, pp. 399–416, 1987.

[34] T. E. Yankeelov and J. C. Gore, "Dynamic contrast enhanced magnetic resonance imaging in oncology: Theory, data acquisition, analysis, and examples," *Curr. Med. Imag. Rev.*, vol. 3, pp. 91–107, 2009.

[35] S. Zwick et al., "Assessment of vascular remodeling under antiangiogenic therapy using DCE-MRI and vessel size imaging," *J. Magn. Reson. Imag.*, vol. 29, pp. 1125–33, 2009.